Early warning for great earthquakes from characterization of crustal deformation patterns with deep learning

J-T., Lin[1], D. Melgar[1], A. M. Thomas[1], and J. Searcy[2]

[1]Department of Earth Sciences, University of Oregon, Eugene, Oregon, USA

[2]Research Advanced Computing Services, University of Oregon, Eugene, Oregon, USA

Corresponding author: Jiun-Ting Lin (jiunting@uoregon.edu)

This is a non-peer reviewed preprint submitted to EarthArXiv. This paper has been submitted to the Journal of Geophysical Research – Solid Earth for review.

Early warning for great earthquakes from characterization of crustal deformation patterns with deep learning

J-T., Lin[1], D. Melgar[1], A. M. Thomas[1], and J. Searcy[2]

[1]Department of Earth Sciences, University of Oregon, Eugene, Oregon, USA

[2]Research Advanced Computing Services, University of Oregon, Eugene, Oregon, USA

Corresponding author: Jiun-Ting Lin (jiunting@uoregon.edu)

Abstract

Although infrequent, large earthquakes (Mw8+) can be extremely damaging and occur on subduction and intraplate faults worldwide. Earthquake early warning (EEW) systems aim to provide advanced warning before strong shaking and tsunami onsets. These models estimate earthquake magnitude by the early metrics of waveforms, relying on empirical scaling relationships of abundant past events. However, both the rarity and complexity of great events make it challenging to characterize them, and EEW algorithms often underpredict magnitude and the resulting hazards. Here we propose a model, M-LARGE, that leverages the power of deep learning to characterize crustal deformation patterns of large earthquakes in real time. We generate realistic rupture scenarios and use these to train a model that directly measures earthquake magnitude from ground displacements. M-LARGE successfully performs reliable magnitude estimation on the testing dataset with an accuracy of 99% for simulated events and for five damaging historical earthquakes in the Chilean Subduction Zone. Unlike existing models which focus on the final earthquake magnitude, M-LARGE tracks the evolution of the source process and can make faster and more accurate magnitude estimates, frequently before rupture is complete. M-LARGE significantly outperforms currently operating EEW algorithms.

1 Introduction

Following earthquake initiation, most EEW algorithms provide the initial hazard predictions based on the character of the first arriving P-waves, which is the earliest information available. However, it is well known that this approach will routinely struggle during large magnitude earthquakes owing to magnitude saturation, or underestimation, a current limitation of such EEW systems. Saturation occurs for two reasons. First, inertial-based instruments (seismometers) that record earthquakes in the near-field tend to distort large, low-frequency, typically over tens to hundreds of seconds, signals radiated from large earthquakes, making the data unreliable (Boore & Bommer, 2005; Larson, 2009; Bock & Melgar, 2016). Second, large earthquakes have durations of several minutes and early onset signals (i.e. the first few seconds) might not contain enough information to forecast the final earthquake magnitude (Rydelek & Horiuchi, 2006; Meier et al., 2016, 2017; Melgar & Hayes, 2017; Ide, 2019; Goldberg et al., 2019). As an example of this, the Japanese EEW system mis-identified the 2011 Mw9.0 Tohoku-oki earthquake as only an Mw8.1 for the first hour after rupture (Hoshiba et al., 2011). This magnitude saturation has consequences for downstream applications that rely on rapid magnitude determination, specifically, in the 2011 Tohoku-oki case both forecasts of the expected shaking and the tsunami amplitudes were drastically underpredicted (Colombelli et al., 2013; Hoshiba et al., 2014).

In recent years, a number of EEW algorithms that attempt to ameliorate the magnitude saturation problem have been developed and tested. For example it is possible to match shaking patterns in real-time to the expected geometric extension of the causative fault (Böse et al., 2012; Hutchison et al., 2020). Another approach is to forego complete characterization of the earthquake, and simply take the observed shaking wavefield at a particular instant in time, and forecast its time-evolution into the future (Kodera et al., 2018; Cochran et al., 2019). Furthermore, the advent of widespread high rate global navigation satellite system (HR-GNSS) networks have

enabled a new class of EEW algorithms based on measurements of crustal deformation and are particularly well suited to identifying large magnitude earthquakes (Crowell et al., 2013; Grapenthin et al., 2014; Minson et al., 2014; Kawamoto et al., 2016). Noteworthy among these are methods is the Geodetic First Approximation of Size and Time (GFAST) algorithm which is primarily based on the scaling of peak ground displacement (PGD) and is currently operating in U.S. EEW system for large earthquakes (Crowell et al., 2013, 2016).

Despite the sophistication of these existing algorithms, many of which are employed in some of the most advanced EEW systems world wide (such as the U.S. and Japan) (Murray et al., 2018; Kodera et al., 2020), each of them has limitations. For example, the seismic wavefield-based approaches overcome saturation at the expense of short warning times, typically of the order of ~10-20s (Kodera et al., 2018). Meanwhile, PGD-based approaches avoid saturation but can struggle when earthquakes have very long or unilateral ruptures (Williamson et al., 2020) and can grossly over-predict the magnitudes of these kinds of events. At the root of these difficulties is that every large earthquake is different from the next. Each can, and likely will, have a different starting location, rupture velocity, slip distribution, and radiated seismic energy that evolves in a complex way as the rupture unfolds. All of these properties fundamentally affect EEW system performance and are difficult if not impossible to predict prior to earthquake occurrence. As such, developing algorithms that can reliably characterize this complexity from surface observations in real-time has proven challenging.

In spite of this diversity of earthquake characteristics, advances in seismic and geodetic instrumentation over the last 30 years have allowed observation and synthesis of the basic kinematic behaviors of large ruptures (Vallée & Douet, 2016; Ye et al., 2016; Hayes, 2017). Additionally, the location and geometry of the faults on which many large earthquakes are expected to occur are well known (Hayes et al., 2018). By combining these observations it is now

possible to efficiently simulate the rupture process of many potential earthquakes in a realistic way, and to predict their expected seismic and geodetic signatures (Melgar et al., 2016; Frankel et al., 2018; Goldberg & Melgar, 2020; Pitarka et al., 2020).

Another important improvement, specifically in the case of HR-GNSS, is that noise models for real-time data have been proposed (Geng et al., 2018; Melgar et al., 2020). HR-GNSS displacements are a derived product and there can be significant differences between real-time and post-processed solutions. This improvement enables adding realistic noise to any simulated waveform. In aggregate, this ability to efficiently simulate data from large earthquakes enables the use of deep learning algorithms (LeCun et al., 2015) that have been demonstrated to provide significant improvements in other data-rich seismological applications such as earthquake detection, phase picking, and association (Perol et al., 2018; Ross et al., 2018; Kong et al., 2019; Zhu & Beroza, 2019; Mousavi et al., 2020a, 2020b). Here, we will show how to leverage the powerful ability of deep-learning together with the aforementioned realistic earthquake simulations and their associated HR-GNSS waveforms to characterize earthquake magnitude in real-time. As a demonstration, we apply this approach to the Chilean Subduction Zone which has a dense real-time GNSS network and assess its performance on five recent large-magnitude earthquakes that have occurred there (Figure 1).

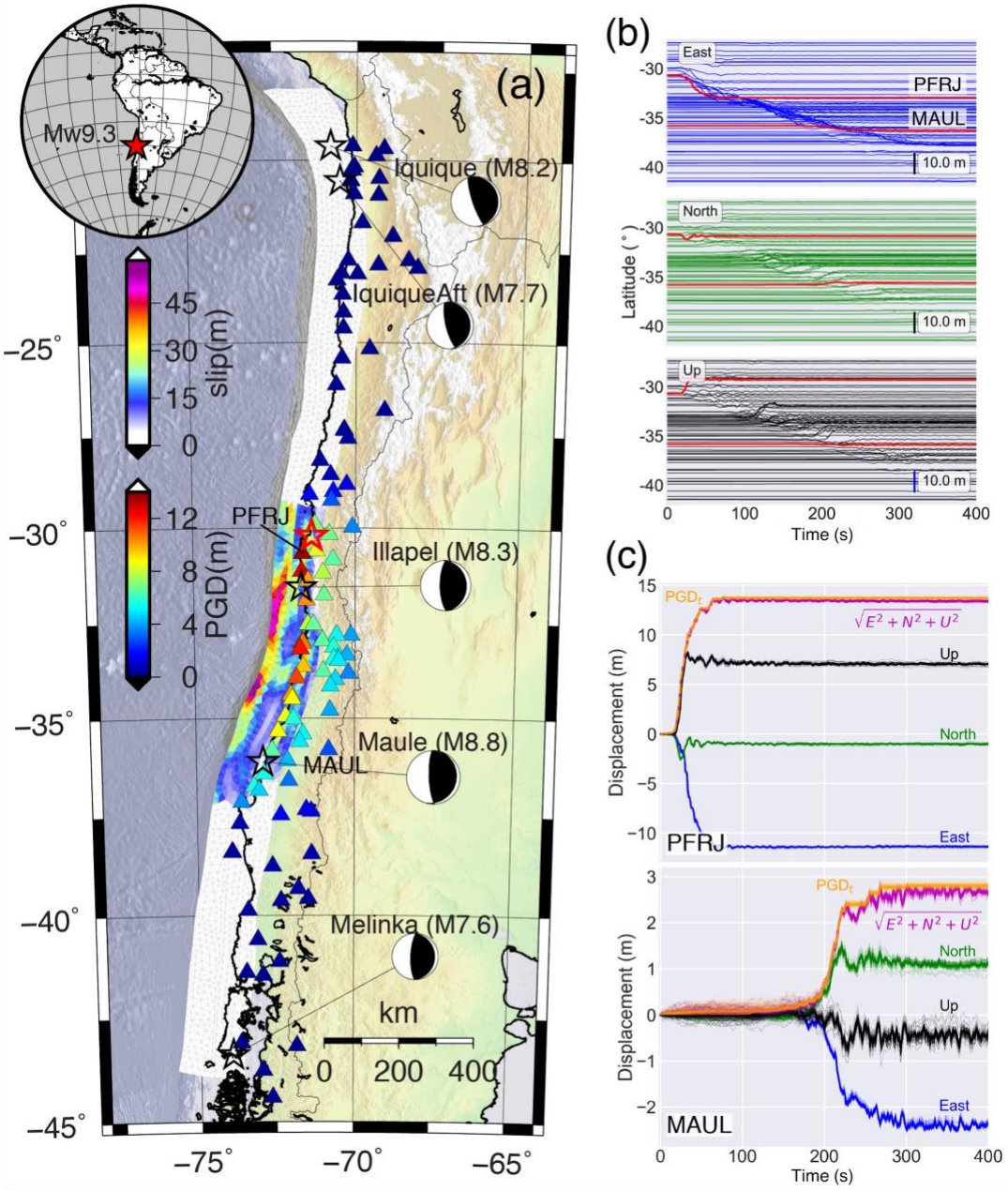

Figure 1. *Map of the Chilean subduction zone, example rupture scenario, and resulting HR-GNSS waveforms. (a) Slip distribution of a Mw9.3 earthquake. GNSS stations (triangles) colored by their PGD. Focal mechanisms of 5 large events that have occurred since 2010. Red and black stars represent the hypocenter of the Mw9.3 rupture scenario and of the historical earthquakes, respectively. (b) Three-component GNSS time series sorted by latitude. Bold red lines denote the records at station PFRJ and MAUL. (c) close-up of time series at stations PFRJ and MAUL. Thin lines denote the GNSS noise introduced in the Data and Method section (see section 2.1).*

2 Data and Methods

2.1 M-LARGE : Model architecture and training

For time-dependent earthquake magnitude prediction we employ a deep-learning model, called Machine Learning Assessed Rapid Geodetic Earthquake magnitude (M-LARGE). It is composed of seven fully connected layers and a unidirectional long-short term memory (LSTM) recurrent layer (Hochreiter & Schmidhuber, 1997), which iteratively predicts Mw using the current and previous HR-GNSS observations across the network (Figure 2; Table 1; see section 2.4 for details). We adopted this model architecture because it is flexible enough to capture the complexities of large earthquakes, allows M-LARGE to update magnitude predictions as the rupture progresses, and it does not require *a-priori* source information (such as the hypocenter) typically required by other rapid modeling methods (e.g. Crowell et al., 2018).

M-LARGE is composed of seven dense (fully connected) layers wrapping an LSTM layer. Note that the dense layers only connect the feature values at the same time channel, rather than all the features, which would include future times as well. Dropouts are applied to prevent overfitting during the training process (Srivastava et al., 2014). We use a Leaky ReLU function with a slope of 0.1 at negative values (Mass et al., 2013), an adaptation of the regular ReLU (Glorot et al., 2011) for the activation for dense layers. Finally, the last layer is connected to a ReLU function to output a current magnitude prediction, and the goal is to minimize the mean square error (MSE) contributed from the magnitude misfits at every epoch (Figure 2). We generated 27,200 ruptures (the process is described in the next section) and split them into training (70%), validation (20%) and testing data (10%) (Figure S1, S2). We apply data augmentation by introducing realistic HR-GNSS noise and station incompleteness yielding more than 6 million earthquake and station scenarios used for 50,000 training steps (Figure S3). Details of the HR-GNSS noise and station incompleteness are provided in section 2.2 and section 2.3, respectively. We save the training weights every 5 epochs and use the model which has the

minimum validation loss as the best model. The code base is publically available and can be obtained at https://github.com/jiunting/MLARGE (Version 1.0.0; Lin, 2021).

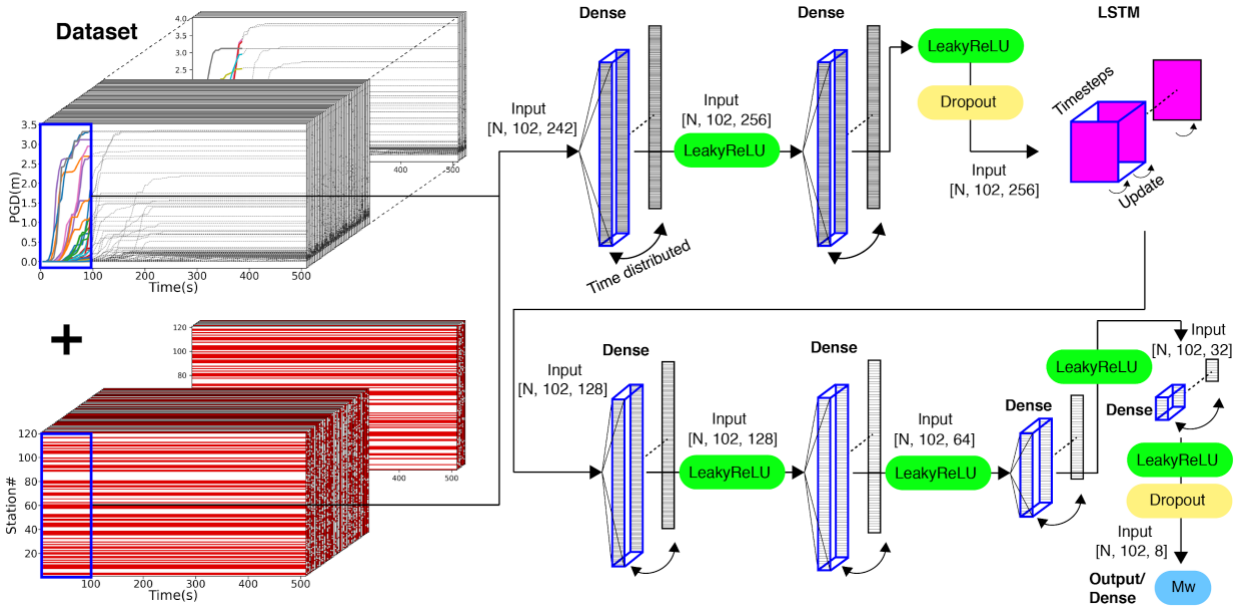

Figure 2. *M-LARGE model architecture showing the input as the time-dependent PGD values from the GNSS stations plus the station on or off (existence) codes. Detailed parameter values are listed in Table 1. Blue rectangles mark the input PGD time series (i.e. 100 s) from all the available stations with their existence codes, and the participating layers.*

Table 1. List of parameter values used

Layer#	Name	Neurons/parameters	Input dimension	Output dimension
Layer0	Input	0	[N, 102, 242]	[N, 102, 242]
Layer1	Dense	256	[N, 102, 242]	[N, 102, 256]
Activation	LeakyReLU	0.1	[N, 102, 256]	[N, 102, 256]
Layer2	Dense	256	[N, 102, 256]	[N, 102, 256]
Activation	LeakyReLU	0.1	[N, 102, 256]	[N, 102, 256]

Layer3	Dropout	0.2	[N, 102, 256]	[N, 102, 256]
Recurrent input				
Layer4	LSTM	128	[N, 102, 256]	[N, 102, 128]
Layer5	Dense	128	[N, 102, 128]	[N, 102, 128]
Activation	LeakyReLU	0.1	[N, 102, 128]	[N, 102, 128]
Layer6	Dense	64	[N, 102, 128]	[N, 102, 64]
Activation	LeakyReLU	0.1	[N, 102, 64]	[N, 102, 64]
Layer7	Dense	32	[N, 102, 64]	[N, 102, 32]
Activation	LeakyReLU	0.1	[N, 102, 32]	[N, 102, 32]
Layer8	Dense	8	[N, 102, 32]	[N, 102, 8]
Activation	LeakyReLU	0.1	[N, 102, 8]	[N, 102, 8]
Layer9	Dropout	0.2	[N, 102, 8]	[N, 102, 8]
Layer10	Dense	1	[N, 102, 8]	[N, 102, 1]

2.2 Rupture scenarios and synthetic waveforms

The Chilean Subduction Zone on the west coast of South America is nearly 3000 km long and accommodates 78-85mm/yr of convergence between the Nazca and South American plates (DeMets et al., 2010). It regularly hosts large magnitude earthquakes including five Mw7.6+ events in the last 10 years (Riquelme et al., 2018). Chile has a real-time HR-GNSS network with more than 120 stations currently in operation (Báez et al., 2018), and provides an excellent testbed for our proposed approach.

For generating the kinematic ruptures we use the Slab2.0 3D slab geometry of (Hayes et al., 2018). We utilize the Chilean slab model from its southern terminus to ~100 km north of the

Chile/Peru border. We limit the seismogenic depth to 55 km consistent with the down-dip extent of recently observed large earthquakes (Ruiz & Madariaga, 2018). The resulting geometry spans a nearly 3000 km long, and 200 km wide fault. The entire fault is then gridded into a total of 3075 triangular subfaults using a finite element mesher, the average length and width of the subfault vertices is ~12 km.

From this global megathrust geometry we generate the 27,200 ruptures (Figure S1) which span the magnitude range Mw7.4 to Mw9.6 using the stochastic approach first described by Graves & Pitarka (2010) with modifications proposed by LeVeque et al., (2016) to avoid the use of Fourier transformations. The magnitudes of the scenarios are uniformly distributed; we generate the same number of earthquakes for each magnitude bin. The goal here is not to obey the Guttenberg-Richter frequency magnitude distribution but rather to generate a meaningful large and varied number of ruptures to expose M-LARGE to a sufficient variety of sources. The process of generating one particular rupture and its associated waveforms is described in detail in Melgar et al. (2016) and is summarized here: once the target magnitude is selected, we define the length and width of fault for that particular rupture. We make a random draw from a probabilistic length, *L*, and width, *W*, scaling law (Blaser et al., 2010). L and W are obtained from a random draw from the lognormal distributions

$$log(L) \sim N(-2.37 + 0.57M_w, \sigma_L) , \quad (1)$$

$$log(W) \sim \boldsymbol{N}(-1.86 + 0.46M_w, \sigma_W) , \quad (2)$$

with standard deviations defined in the original work of Blaser et al. (2010). The objective is to obtain a length and width that is consistent with the behavior seen in earthquakes worldwide while retaining the observed variability as well. The probabilistic scaling law thus ensures that for a

given magnitude we do not always employ the same fault dimensions. Detailed statistics on the resulting fault dimensions for all simulated ruptures can be seen in Figure S1. Once the fault dimensions are defined, we select a location on the megathrust at random to locate this rupture on. This also promotes larger source complexity due to larger variation of the hypocenter-centroid separation for large events (Figure S4). Here we do not take into account the variability in along-strike plate convergence rates or any information pertaining to which parts of the megathrust are considered more or less likely to experience a rupture. Rather, as with the magnitude definition, by keeping a uniform probability across the megathrust we are simply attempting to generate a diverse enough set of ruptures to expose the machine learning algorithm to.

Having selected the portion of megathrust we next generate the slip pattern and GNSS waveforms. For this we use the Karhunen-Loeve (KL) expansion method (LeVeque et al., 2016, Melgar et al., 2016;). The process is separated into the following three main steps: 1) generate the stochastic slip patterns, 2) define rupture kinematics, and 3) forward synthesis of GNSS waveforms using a Green's function approach. Detailed processes are provided in the Text S1 in the supporting information. Finally, to make the synthetic data more realistic, we introduce noise into the displacement waveform characteristics using a known real-time GNSS noise model (Melgar et al., 2020) which was computed from analysis of one year-long real HR-GNSS observations spanning a large region. The reference noise model provides expected spectra of noise that vary from the 1st percentile or "low" noise model, continuously through the 50th percentile "median" noise model and up to the 90th percentile "high" noise model. For each waveform we randomly select the percentile noise model and add it to the displacement data. It's worthwhile noting that we only assume the amplitude spectrum of noise, we keep the phase spectrum random. This guarantees that for a specific noise amplitude model the resulting time-domain waveform varies with each realization. In this way we guarantee a large variability of noise and quality in the stations as is routinely seen in true real-time operations.

To ensure that the waveforms are realistic, we validate the HR-GNSS by comparing the simulated peak ground displacement against what is expected from PGD-Mw scaling (Melgar et al., 2015; Ruhl et al., 2019). This is shown in Figure S5, we find that the synthetic PGD pattern matches the scaling based on real observations at hypocentral distance ~100 km and Mw from Mw7.7 to Mw8.7. We note that misfit between modeled and expected values of PGD increases at Mw greater than Mw9.0 or hypocentral distance smaller than 10km. This has been noted before in Melgar et al. (2016) and is due to the fact that the PGD regressions are constructed from databases of real events; large earthquakes (i.e. Mw9.0+) and very close observations are comparatively rare in those databases. The larger misfit is also due to the point source assumption in PGD-Mw scaling laws. All the resulting synthetic data is publicly available on Zenodo (https://zenodo.org/record/4008690) (Dataset; Lin et al., 2020).

2.3 M-LARGE: PGD features and Mw labeling

To rapidly determine Mw in real time, we train M-LARGE by linking the input PGD time series recorded at each GNSS station to the time dependent Mw for each rupture derived from integration of the source time function (STF). PGD time series is calculated from

$$PGD(t) = max\left(\sqrt{E(t)^2 + N(t)^2 + Z(t)^2}\right), \quad (3)$$

where *E(t)*, *N(t)*, *Z(t)* represents the East, North and vertical component of the GNSS displacement time series starting from the earthquake origin (i.e. t=0), respectively. We introduce feature scaling, which is commonly applied in machine learning, to avoid large feature values dominating smaller ones, making the model convergence difficult. The PGD time series is first clipped at a minimum of 0.02m and scaled logarithmically. This is done so that during this re-

scaling process the zero-valued data do not diverge to negative infinity. We add an additional "station existence" feature channel for every station to distinguish the difference between a very small value and no data from a simulated station outage. We set the code to zero to simulate a station malfunction due to an outage, and set it to 0.5 if the station is working normally. We decimate all the time series to 5 second sampling so that we obtain Mw updates in 5 second increments. A total of 121 stations (Figure 1) with their corresponding existence codes, and 102 time steps (i.e. 5 s sampling for 510 s of signal duration) of data are used. Data incompleteness is included by randomly removing stations up to a maximum of 115 stations (i.e. a minimum of only 6 stations remaining). We also set a minimum threshold so that at least 4 stations are located within 3 degrees from the hypocenter. This is to make sure that the removal of training data still carries some near-field information, otherwise the algorithm may introduce a bias because of the similar far-field values but different labeled magnitudes. Note that the hypocenter is the only necessary information for data augmentation. During the training process, no hypocenter information is needed. Here we also note that M-LARGE does not detect the onset of an event. GNSS data is noisy enough that event detection from the real-time data can lead to many false positives (Kawamoto et al., 2016). Rather M-LARGE requires triggering, ostensibly by a seismic system as is common in other GNSS algorithms (e.g. Crowell et al., 2018). The noise in GNSS data is greater than that in seismic data and many algorithms have been demonstrated for detection of the onset of events using inertial recordings (Perol et al., 2018; Ross et al., 2018; Zhu & Beroza, 2019) so a system that relies on seismometers for triggering is still the most robust.

For the Mw labeling, we use the time integration from the real STF, convert it to the moment magnitude scale, and re-scale this by dividing the resulting value by 10 for computational efficiency. One assumption we have made is that there is no travel time delay due to the propagation of seismic waves from source-to-station in the feature and label pair. Although the feature and the Mw label should theoretically have a delay term, we consider this a neglectable

misfit in the model. In fact, the misfit is only a small portion at the beginning of the sequence considering the whole 510 s of long time series, and the algorithm seems to address this properly to predict the non-delayed label after more incoming data are available. This non-delayed prediction continues until the rupture termination and information has completely propagated to stations when the real data and Mw label synchronize with each other.

2.4 GFAST and GPSCMT

Our main point of comparison for assessing whether M-LARGE is an improvement will be GFAST (Crowell et al., 2016), which is one of the most stable GNSS EEW methods and is currently operating in the U.S. EEW system (i.e. ShakeAlert). It uses the PGD observations from HR-GNSS time series. When a hypocenter is confirmed by a seismic method, the magnitude is calculated based on the PGD-Mw scaling relationship (Crowell et al., 2016; Melgar et al., 2015; Ruhl et al., 2019). To ensure the data contain PGD information and not noise, a 3 km/s travel-time filter is added into the algorithm, and the model only predicts Mw when at least 4 stations have valid information.

GFAST is not the only GNSS modeling approach, there are other proposed algorithms that utilize near-field GNSS data to rapidly estimate earthquake magnitude. To further compare with M-LARGE we also run the Global Positioning System based centroid moment tensor (GPSCMT) method, which utilizes the near-field static offset term from the GNSS records to calculate magnitude, moment tensor and centroid location (Melgar et al., 2012; Lin et al., 2019). Unlike the GFAST approach, GPSCMT does not require hypocenter information, instead it grid-searches every pre-built centroid location, solves for the moment tensor and finds the preferred location which has the minimum residual. We take the same subfault meshes used by M-LARGE, used to generate rupture scenarios, as the potential centroid locations. Both the performance of GFAST and GPSCMT are shown in the next section.

3 Results

3.1 M-LARGE performance on testing dataset

The performance of M-LARGE on the testing dataset is shown in Figure 3. We define a correct prediction as one within +/-0.3 units of the target magnitude (i.e. time-dependent magnitude) and calculate the model accuracy (Figure 3b, Figure S6a in the supporting information). Within these bounds, the model performs well with a high accuracy of 96% after 60 s which increases to 99% by 120 s. The standard deviation of the magnitude misfits are 0.14, 0.1, 0.09 at 60, 120, and 240 s, respectively. We compare this statistic to the GFAST algorithm by using the same testing dataset as M-LARGE. Note that for GFAST, we remove those predictions with Mw=0 due to the four station minimum thresholding and only show the data that have predicted values (Figure 3b). Despite this, we find that GFAST has a longer determination time and lower accuracy of 60% at 60 s which slowly increases to 88% by 240 s. In comparison to M-LARGE, GFAST's accuracy saturates at 88.1% by 255 seconds. The standard deviation of the magnitude predictions of GFAST are also larger 0.23, 0.19, 0.18 at 60, 120, 240 s, respectively, about 2 times more scatter than the M-LARGE performance. To summarize, M-LARGE reaches 80% accuracy 5 times faster than GFAST and has half the scatter on average.

Furthermore, we compare the performance between M-LARGE and the GPSCMT (Figure. S7). Again, M-LARGE significantly outperforms the GPSCMT, where the accuracies are 40%, 25% and 24% at 60, 120, 240 s, respectively. Noting that the GPSCMT performs with overall much larger scatter, lower accuracy, and systematic overestimations. This has been noted before, that a point source has limited ability on recovering the deformation of large offshore events (e.g. Melgar et al., 2013). Thus, without additional constraints, the model accuracy of GPSCMT method is about 40% according to our testing dataset.

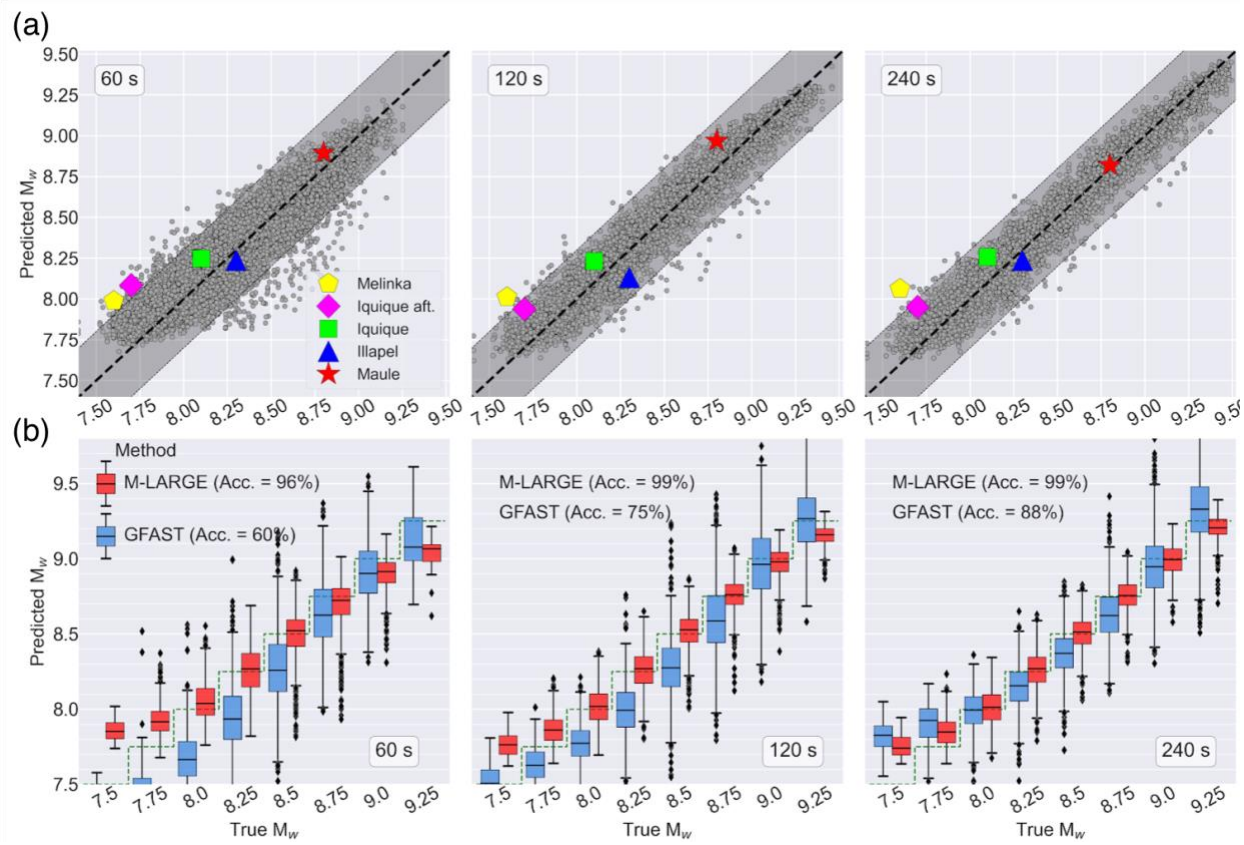

Figure 3. *Model performance on testing dataset and on real events. (a) (from left to right) snapshots of the M-LARGE performance at 60, 120, 240 s, respectively. Gray dots show the Mw predictions compared to the time-dependent magnitude. Black dashed line represents the 1:1 line; shaded area represents the* ± 0.3 *magnitude range. Colored markers denote the M-LARGE predicted Mw and their final Mw for 5 real events in Figure 1. (b) comparison of the GFAST (blue) and M-LARGE (red) predicted magnitudes at 60,120 and 240 s for different magnitude bins. Model accuracies at 60, 120 and 240 s are shown in text. The green dashed line is the 1:1 reference for each magnitude bin.*

3.2 M-LARGE performance on real large earthquakes

To further assess the performance of M-LARGE, we apply the model to five large historical events in the Chilean Subduction Zone with HR-GNSS records which are not employed in training (Figure 4). For each of these earthquakes different numbers of GNSS sites were available. For

the 2010 Mw8.8 Maule earthquake the model only takes 40 s to reach the +/-0.3 magnitude unit criteria. M-LARGE also successfully predicts the final magnitude of the 2014 Mw8.1 Iquique and the 2015 Mw8.3 Illapel earthquakes at 20 s and 35 s, respectively. For the 2014 Mw7.7 Iquique aftershock and the 2016 Mw7.6 Melinka earthquakes, the M-LARGE predictions both overshoot the true magnitude at 30 s, but soon correct downward. We also note that the performance statistics are quoted from the event origin time and include delay times prior to the P-wave arrival at the closest stations. In most events the first arrival occurs by 20 s, and only 6% of rupture scenarios have arrivals later than 20 s. For the Maule earthquake, where most of the presently operating closest stations did not exist, the first arrival times are 17 s. Considering these delay times, useful predictions are made as soon as the signals are recorded but the lowest uncertainties are anticipated after ~30 s. This can be seen in Figure 4 and Figure S6, where lower uncertainties occur in the later predictions.

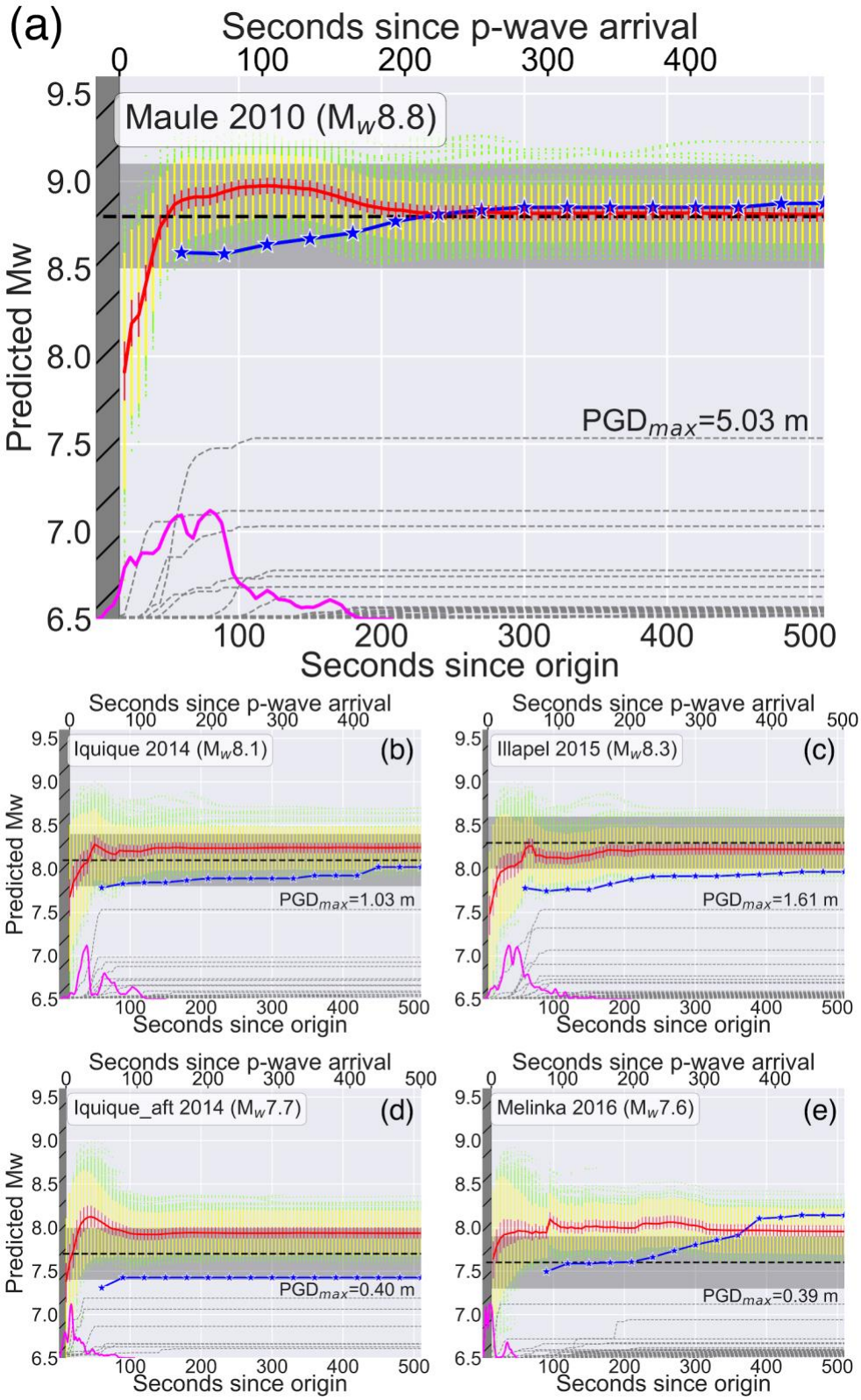

Figure 4. *M-LARGE performance on real Chilean earthquakes. (a) The 2010 Maule Mw8.8 earthquake. Black dashed line and gray shaded areas represent the true Mw and the +/-0.3 magnitude unit range. Red*

line shows the M-LARGE predicted Mw, with the boxes (red bars) and whiskers (yellow bars) denoting the 50% and 99.7% of the target Mw population, respectively. Green dots represent outliers. Blue stars show the GFAST prediction given the same data used by M-LARGE. Thin dashed lines show the PGD waveforms from the GNSS network (Figure 1). Magenta line represents the event source time function from the USGS finite fault. Hatched dark gray area is the time period prior to the arrival of the P-wave at the closest site where no information on the rupture is available. (b)-(e) Same as (a) but for the 2014 Mw8.1 Iquique earthquake, the 2015 Mw8.3 Illapel earthquake, the 2014 Mw7.7 Iquique aftershock, and the 2016 Mw7.6 Melinka earthquake, respectively.

3.3 M-LARGE performance on imperfect data

Given the limited availability of real events, it is important to investigate how M-LARGE performs on imperfect data. First, we test the M-LARGE on two different recording scenarios on the same rupture with one having poor station coverage versus well coverage for the other one (Figure 5). In the poor station coverage example (i.e. Case 1 in Figure 5), almost all the near-field data are missing and M-LARGE is only able to successfully estimate magnitude after 230 s, when far field stations begin recording data and M-LARGE upgrades its moment estimate (Figure 5b, 5c). In contrast, in the second example, abundant near-field data is used to accurately characterize the rupture process and M-LARGE predicts the actual magnitude in 120 s (Figure 5b, 5d). This suggests that data sparsity in the near-field plays the most important role for the accuracy and timeliness of the predictions. The clear implication is that having more stations closer to the source improves M-LARGE's performance.

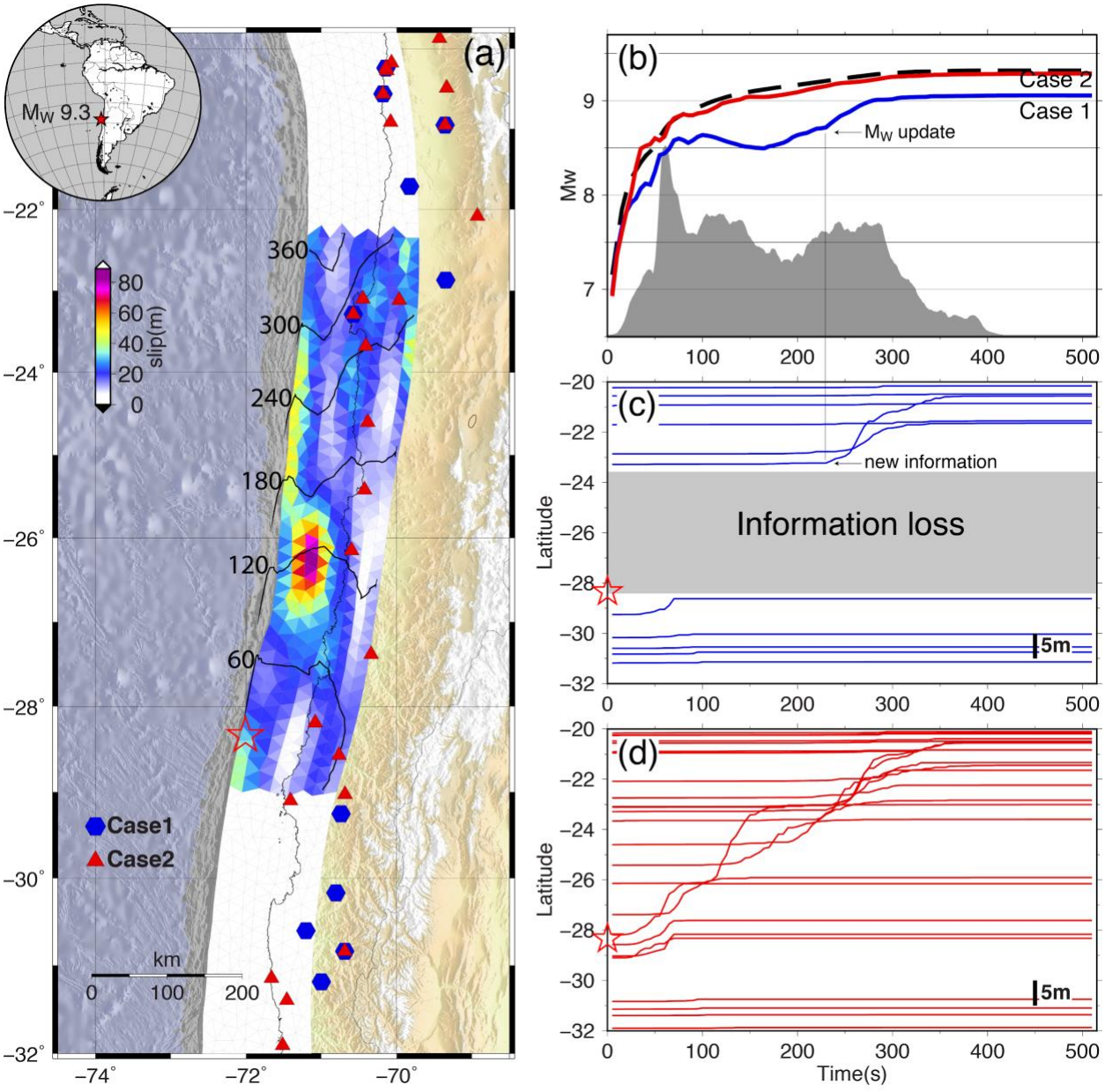

Figure 5. *M-LARGE prediction tests with different station distributions. (a) rupture scenario of a Mw9.3 earthquake with the station distribution of Case1 (blue hexagon) and Case2 (red triangle). Black lines with numbers show the rupture time contours. (b) M-LARGE predictions for Case 1 (blue line), Case 2 (red line) and the actual Mw (dashed line) calculated from the STF (gray area). (c) PGD data of Case 1 sorted by latitude, Red star denotes the hypocenter latitude. (d) similar to (c), but data of Case 2.*

3.4 M-LARGE performance on different source time function types

To examine the M-LARGE performance as a function of source complexity, we choose four different characteristic source time function shapes (i.e. symmetric, bimodal, early and late skewed) and analyze the results. Figure 6 shows examples of each of these characteristic STFs, we find that the complexity of the time dependent moment evolution does not affect the accuracy of the M-LARGE estimations because it is trained to map the actual STF directly.

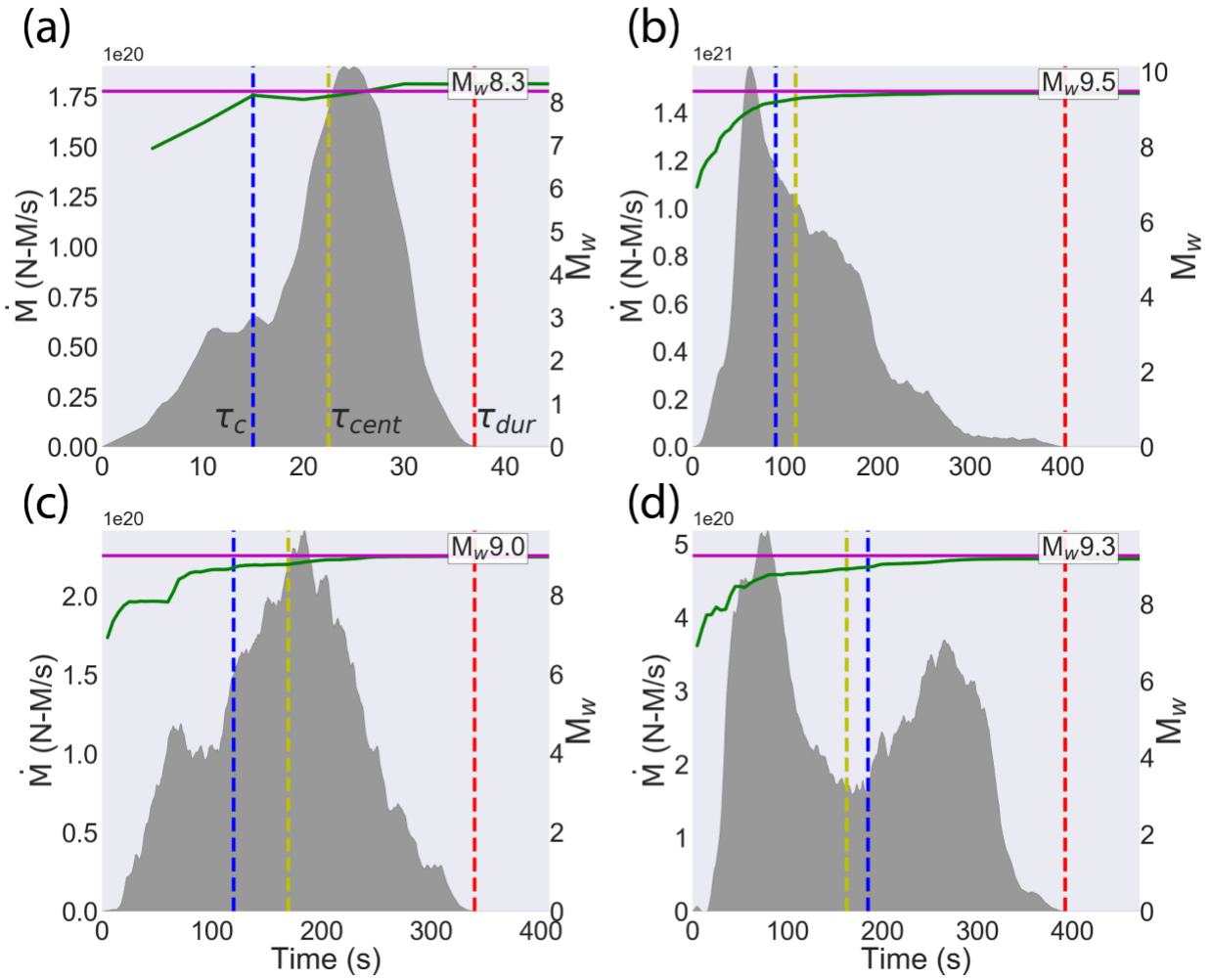

Figure 6*. Example plot for the τ_c(time to corrected prediction), τ_{cent}(centroid time), τ_{dur}(duration). Green and magenta line shows the M-LARGE prediction and final magnitude, respectively. (a) shows the case of late rupturing, where the source focuses at the end of the rupture. (b) shows the case with early rupturing, where the source focuses at the beginning of the rupture. (c) nearly symmetric (triangular) source time function. (d) shows the case of two rupture asperities.*

4. Discussion

4.1 Earlier final magnitude estimation

Although the timeliness of the final magnitude assessment is intimately tied to the evolution of the STFs (i.e. whether the event grows faster or slower), we find that the final magnitude can, on average, still be predicted by 20%-40% of the rupture duration time (Figure 7a). This earlier prediction of M-LARGE is in part due to our definition of correct prediction (i.e. +/-0.3 magnitude unit). Based on the Mw-duration scaling of Duputel et al. (2013), an -0.3 magnitude unit earthquake can be estimated by 71% of the original duration time (a detailed derivation is provided in the Test S2 in the supporting information). For example, on average, a Mw9.0 event takes ~170 s to rupture, while it only takes 120 s to rise to the acceptable Mw threshold of Mw8.7. In this case, a final prediction can be made before the rupture termination providing a shortcut to practical warning, and this is only possible when the real-time STF can be accurately measured. However, this only accounts for 71 % of the original duration. Additionally to explain the faster magnitude estimation time, which is 20%-40% of duration, we find that the M-LARGE's real-time STF is likely leveraging some degree of the weak determinism (Meier et al., 2017; Goldberg et al., 2018; Melgar & Hayes, 2019) that is present, on average, in the training data and in the Chilean events used for final validation. For example, the Mw8.8 Maule earthquake converges to its correct magnitude even before the peak moment rate in the source time function (Figure 4a) and the duration of the acceptable +/-0.3 Mw range (i.e. Mw8.5 takes ~95 s to rupture). When exactly, during the rupture process, final earthquake magnitude can be determined is still debated in the earthquake science community. The end member views are that earthquakes are strongly deterministic (Wu & Zhao, 2006; Olson & Allen, 2005), i.e. information about the final magnitude is contained in the signals from the first seconds following nucleation of the event; and that they are not deterministic at all (Rydelek & Horiuchi, 2006; Ide, 2019), i.e. magnitude cannot be determined before the rupture is complete. We note here that we have not explicitly assumed

any determinism in the generation of our synthetic rupture scenarios used to train M-LARGE. Instead, our training models have growth patterns that behave according to what is seen in worldwide databases (Figure 7b). That said, any individual rupture scenario may depart from this average behavior (i.e. see Figure S8 in the supporting information) and ultimately the success of M-LARGE is contingent on how representative the training data is of real large magnitude earthquakes. In sum, the model learns some degree of determinism of the earthquake source, facilitating faster final magnitude prediction.

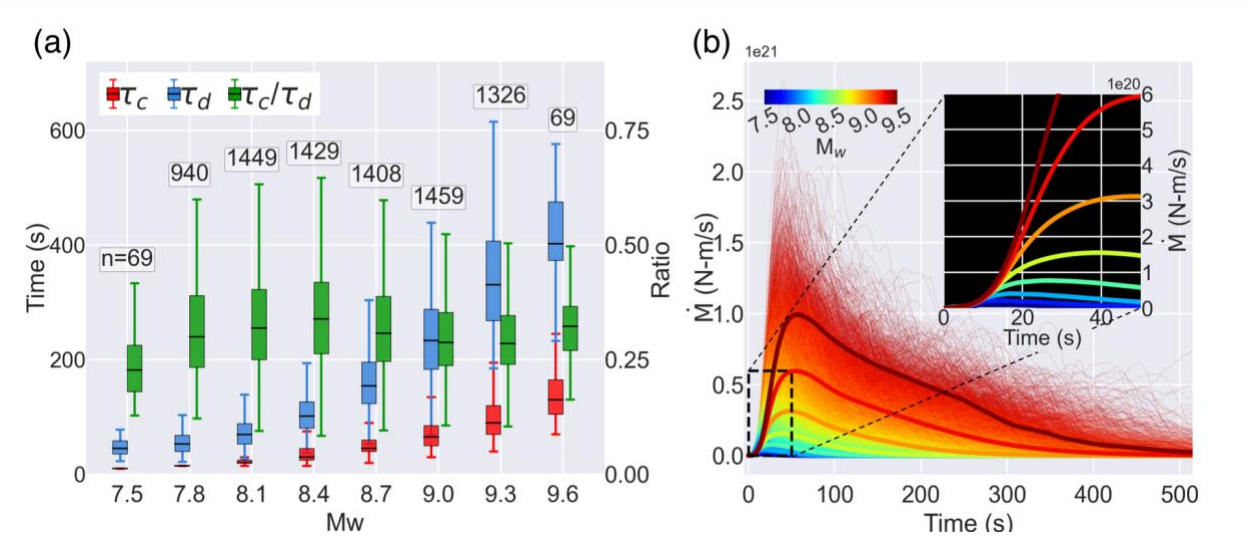

Figure 7. *Warning time ratios and STF analysis. (a) shows the duration (τ_d), time to the correct prediction (τ_c), and the ratio between these two for each magnitude bin. Texts indicate the number of samples for each bin. (b) shows the STF of 27200 rupture scenarios color coded by Mw. Thick lines denote the averaged STF of different magnitude bins. Inset shows the zoom-in view of the averaged source time functions.*

4.2 Limitations and future steps

We have shown that M-LARGE has the ability to learn complex rupture patterns from the crustal deformation data. Also, that it significantly outperforms other HR-GNSS algorithms. However, we note that it still has some limitations and these should be targets for potential improvements in

the future. First, once M-LARGE is trained, the model is not global in scope, it is limited by the simulated earthquakes and waveforms for a particular region (i.e. in this study, the Chilean Subduction Zone). Thus, the model needs to be re-trained to adapt to different areas. Although the model can be generalized by introducing feature engineering (e.g. extract the hypocentral distance used by GFAST), we have not attempted to generalize it because regional heterogeneity such as site effects, subduction zone environments and station distribution vary, so global model generalization is non-trivial. However, synthesis of the ruptures and GNSS waveforms is fast enough that re-training for another network or region is not a numerically prohibitive task. Second, we note that for the 2010 Mw8.8 Maule earthquake example, there is a 17 s gap without recording due to lack of near-field stations. This performance could be sped up by ~10 s if the information delay introduced by the travel times could be reduced, i.e. if station coverage could be expanded offshore.

We note that the model architecture and hyperparameters are selected arbitrarily and the scale of hyperparameters are comparable to the similar studies (e.g. Ross et al., 2018; Zhu & Beroza, 2019). Beside the architecture we used (Figure 2), we have also explored the parameter space. However, we do not find significant model improvement on tuning the hyperparameters, probably because the model has already reached its accuracy limit (i.e. 99%) based on the currently designed architecture. Any further improvement will need more delicate model design. We find that the logarithm scaling function of PGD features has better performance against the commonly adopted linear scaling. This is consistent with the existence of logarithm PGD and magnitude relationships (Crowell et al., 2016; Melgar et al., 2015; Ruhl et al., 2019) making the input and output pairs less complicated during model training.

The earthquake magnitude is not the only important factor for EEW. In fact, the source location, rupture length and width are equally important for an accurate ground motion prediction or tsunami amplitude forecast. In this paper, we have successfully demonstrated that M-LARGE is capable of learning Mw directly from raw observations. This is a starting point for this new type of

l EEW algorithm, and we anticipate that, given this success, it is reasonable to infer that M-LARGE can be expanded to learn other source parameters necessary for hazards forecasts.

5 Conclusion

Developing frameworks to provide timely warning during the largest magnitude earthquakes remains an outstanding scientific and technological challenge. EEW systems continue to expand and have proliferated to many countries across the globe (Allen & Melgar, 2019). Despite this, how these systems will perform in rare but high consequence, large magnitude earthquakes is uncertain. Here, we have combined knowledge of where great earthquakes will occur, their average expected rupture characteristics, state of the art sensor technology, and deep learning to rapidly characterize large magnitude earthquakes from their crustal deformation patterns. The resulting EEW algorithm, M-LARGE, has significantly better performance than current algorithms and can readily be generalized to any faulting environment capable of generating large events. As such, M-LARGE represents a new approach to EEW that if made operational, will obviate many of the performance limitations of current technologies providing accurate and fast alerts that will lead to increased resilience.

Data availability

The rupture simulations and waveforms can be found on Zenodo: https://zenodo.org/record/4008690. The code of M-LARGE can be obtained at https://github.com/jiunting/MLARGE.

Acknowledgement

This work is funded by National Aeronautics and Space Administration NESSF grant 80NSSC18K1420 and National Science Foundation grants 1663834 and 1835661. This work is also partially funded by NASA grants 80NSSC19K0360 and 80NSSC19K1104. We thank the Centro Sismologico Nacional of Chile for operation of the HR-GNSS network and access to their data. We would also like to thank Amy Williamson and Brendan Crowell for discussions on the performance of GFAST on simulated events.

References

Allen, R. M., & Melgar, D. (2019), Earthquake early warning: Advances, scientific challenges, and societal needs. *Annual Review of Earth and Planetary Sciences*, *47*, 361-388.

Báez, J. C., Leyton, F., Troncoso, C., del Campo, F., Bevis, M., Vigny, C., ... & Blume, F. (2018), The Chilean GNSS network: Current status and progress toward early warning applications. *Seismological Research Letters*, *89*(4), 1546-1554.

Blaser, L., Krüger, F., Ohrnberger, M., & Scherbaum, F. (2010), Scaling relations of earthquake source parameter estimates with special focus on subduction environment. Bulletin of the Seismological Society of America, 100(6), 2914-2926.

Bock, Y., & Melgar, D. (2016), Physical applications of GPS geodesy: A review. *Reports on Progress in Physics*, *79*(10), 106801.

Boore, D. M., & Bommer, J. J. (2005). Processing of strong-motion accelerograms: needs, options and consequences. *Soil Dynamics and Earthquake Engineering*, *25*(2), 93-115.

Böse, M., Heaton, T. H., & Hauksson, E. (2012), Real-time finite fault rupture detector (FinDer) for large earthquakes. Geophysical Journal International, 191(2), 803-812.

Cochran, E. S., Bunn, J., Minson, S. E., Baltay, A. S., Kilb, D. L., Kodera, Y., & Hoshiba, M. (2019), Event Detection Performance of the PLUM Earthquake Early Warning Algorithm in Southern CaliforniaEvent Detection Performance of the PLUM Earthquake Early Warning Algorithm in Southern California. *Bulletin of the Seismological Society of America*, *109*(4), 1524-1541.

Colombelli, S., Allen, R. M., & Zollo, A. (2013), Application of real-time GPS to earthquake early warning in subduction and strike-slip environments. *Journal of Geophysical Research: Solid Earth*, *118*(7), 3448-3461.

Crowell, B. W., Melgar, D., Bock, Y., Haase, J. S., & Geng, J. (2013), Earthquake magnitude scaling using seismogeodetic data. *Geophysical Research Letters*, *40*(23), 6089-6094.

Crowell, B. W., Schmidt, D. A., Bodin, P., Vidale, J. E., Gomberg, J., Renate Hartog, J., ... & Jamison, D. G. (2016), Demonstration of the Cascadia G-FAST geodetic earthquake early warning system for the Nisqually, Washington, earthquake. Seismological Research Letters, 87(4), 930-943.

Crowell, B. W., Schmidt, D. A., Bodin, P., Vidale, J. E., Baker, B., Barrientos, S., & Geng, J. (2018). G-FAST earthquake early warning potential for great earthquakes in Chile. *Seismological Research Letters*, *89*(2A), 542-556.

DeMets, C., Gordon, R. G., & Argus, D. F. (2010), Geologically current plate motions. *Geophysical Journal International*, *181*(1), 1-80.

Duputel, Z., Tsai, V. C., Rivera, L., & Kanamori, H. (2013). Using centroid time-delays to characterize source durations and identify earthquakes with unique characteristics. *Earth and Planetary Science Letters*, *374*, 92-100.

Frankel, A., Wirth, E., Marafi, N., Vidale, J., & Stephenson, W. (2018), Broadband Synthetic Seismograms for Magnitude 9 Earthquakes on the Cascadia Megathrust Based on 3D Simulations and Stochastic Synthetics, Part 1: Methodology and Overall ResultsMethodology and Overall Results. *Bulletin of the Seismological Society of America*, *108*(5A), 2347-2369.

Geng, J., Pan, Y., Li, X., Guo, J., Liu, J., Chen, X., & Zhang, Y. (2018). Noise characteristics of high-rate multi-GNSS for subdaily crustal deformation monitoring. *Journal of Geophysical Research: Solid Earth*, *123*(2), 1987-2002.

Glorot, X., Bordes, A., & Bengio, Y. (2011), Deep sparse rectifier neural networks. In Proceedings of the fourteenth international conference on artificial intelligence and statistics (pp. 315-323).

Goldberg, D. E., Melgar, D., Bock, Y., & Allen, R. M. (2018), Geodetic observations of weak determinism in rupture evolution of large earthquakes. *Journal of Geophysical Research: Solid Earth*, *123*(11), 9950-9962.

Goldberg, D. E., Melgar, D., & Bock, Y. (2019), Seismogeodetic P-wave amplitude: No evidence for strong determinism. *Geophysical research letters*, *46*(20), 11118-11126.

Goldberg, D. E., & Melgar, D. (2020). Generation and validation of broadband synthetic P waves in semistochastic models of large earthquakes. *Bulletin of the Seismological Society of America*, *110*(4), 1982-1995.

Grapenthin, R., Johanson, I. A., & Allen, R. M. (2014), Operational real-time GPS-enhanced earthquake early warning. Journal of Geophysical Research: Solid Earth, 119(10), 7944-7965.

Graves, R. W., & Pitarka, A. (2010), Broadband ground-motion simulation using a hybrid approach. Bulletin of the Seismological Society of America, 100(5A), 2095-2123.

Hayes, G. P. (2017), The finite, kinematic rupture properties of great-sized earthquakes since 1990. *Earth and Planetary Science Letters*, *468*, 94-100.

Hayes, G. P., Moore, G. L., Portner, D. E., Hearne, M., Flamme, H., Furtney, M., & Smoczyk, G. M. (2018), Slab2, a comprehensive subduction zone geometry model. *Science*, *362*(6410), 58-61.

Hochreiter, S., & Schmidhuber, J. (1997), Long short-term memory. *Neural computation*, *9*(8), 1735-1780.

Hoshiba, M., Iwakiri, K., Hayashimoto, N., Shimoyama, T., Hirano, K., Yamada, Y., ... & Kikuta, H. (2011). Outline of the 2011 off the Pacific coast of Tohoku Earthquake (M w 9.0)—Earthquake Early Warning and observed seismic intensity—. *Earth, planets and space*, *63*(7), 547-551.

Hoshiba, M., & Ozaki, T. (2014), Earthquake Early Warning and Tsunami Warning of the Japan Meteorological Agency, and Their Performance in the 2011 off the Pacific Coast of Tohoku Earthquake (Mw9.0). In *Early warning for geological disasters* (pp. 1-28). Springer, Berlin, Heidelberg.

Hutchison, A. A., Böse, M., & Manighetti, I. (2020), Improving early estimates of large earthquake's final fault lengths and magnitudes leveraging source fault structural maturity information. *Geophysical Research Letters*, e2020GL087539.

Ide, S. (2019), Frequent observations of identical onsets of large and small earthquakes. *Nature*, *573*(7772), 112-116.

Kawamoto, S., Hiyama, Y., Ohta, Y., & Nishimura, T. (2016), First result from the GEONET real-time analysis system (REGARD): the case of the 2016 Kumamoto earthquakes. *Earth, Planets and Space*, *68*(1), 190..

Kodera, Y., Yamada, Y., Hirano, K., Tamaribuchi, K., Adachi, S., Hayashimoto, N., ... & Hoshiba, M. (2018), The propagation of local undamped motion (PLUM) method: A simple and robust seismic wavefield estimation approach for earthquake early warning. *Bulletin of the Seismological Society of America*, *108*(2), 983-1003.

Kodera, Y., Hayashimoto, N., Moriwaki, K., Noguchi, K., Saito, J., Akutagawa, J., ... & Hoshiba, M. (2020), First-Year Performance of a Nationwide Earthquake Early Warning System Using a Wavefield-Based Ground-Motion Prediction Algorithm in Japan. *Seismological Research Letters*, *91*(2A), 826-834.

Kong, Q., Trugman, D. T., Ross, Z. E., Bianco, M. J., Meade, B. J., & Gerstoft, P. (2019). Machine learning in seismology: Turning data into insights. *Seismological Research Letters*, *90*(1), 3-14.

Larson, K. M. (2009), GPS seismology. *Journal of Geodesy*, *83*(3-4), 227-233.

LeCun, Y., Bengio, Y., & Hinton, G. (2015), Deep learning. *nature*, *521*(7553), 436-444.

LeVeque, R. J., Waagan, K., González, F. I., Rim, D., & Lin, G. (2016), Generating random earthquake events for probabilistic tsunami hazard assessment. In Global Tsunami Science: Past and Future, Volume I (pp. 3671-3692). Birkhäuser, Cham.

Lin, J. T., Chang, W. L., Melgar, D., Thomas, A., & Chiu, C. Y. (2019), Quick determination of earthquake source parameters from GPS measurements: a study of suitability for Taiwan. Geophysical Journal International, 219(2), 1148-1162.

Lin, J. T., Melgar, D., Thomas, A., & Searcy, J. (2020). Chilean Subduction Zone rupture scenarios and waveform data [Data set]. Zenodo. http://doi.org/10.5281/zenodo.4008690

Lin, J. T. (2021). jiunting/MLARGE: First release of MLARGE (Version v1.0.0). Zenodo. http://doi.org/10.5281/zenodo.4527253

Maas, A. L., Hannun, A. Y., & Ng, A. Y. (2013), Rectifier nonlinearities improve neural network acoustic models. In Proc. icml (Vol. 30, No. 1, p. 3).

Meier, M. A., Heaton, T., & Clinton, J. (2016), Evidence for universal earthquake rupture initiation behavior. *Geophysical Research Letters*, *43*(15), 7991-7996.

Meier, M. A., Ampuero, J. P., & Heaton, T. H. (2017), The hidden simplicity of subduction megathrust earthquakes. *Science*, *357*(6357), 1277-1281.

Melgar, D., Bock, Y., & Crowell, B. W. (2012), Real-time centroid moment tensor determination for large earthquakes from local and regional displacement records. Geophysical Journal International, 188(2), 703-718.

Melgar, D., Crowell, B. W., Bock, Y., & Haase, J. S. (2013), Rapid modeling of the 2011 Mw 9.0 Tohoku-Oki earthquake with seismogeodesy. *Geophysical Research Letters*, *40*(12), 2963-2968.

Melgar, D., Crowell, B. W., Geng, J., Allen, R. M., Bock, Y., Riquelme, S., ... & Ganas, A. (2015), Earthquake magnitude calculation without saturation from the scaling of peak ground displacement. Geophysical Research Letters, 42(13), 5197-5205.

Melgar, D., LeVeque, R. J., Dreger, D. S., & Allen, R. M. (2016), Kinematic rupture scenarios and synthetic displacement data: An example application to the Cascadia subduction zone. *Journal of Geophysical Research: Solid Earth*, *121*(9), 6658-6674.

Melgar, D., & Hayes, G. P. (2017), Systematic observations of the slip pulse properties of large earthquake ruptures. *Geophysical Research Letters*, *44*(19), 9691-9698.

Melgar, D., & Hayes, G. P. (2019), Characterizing large earthquakes before rupture is complete. *Science Advances*, *5*(5), eaav2032.

Melgar, D., Crowell, B. W., Melbourne, T. I., Szeliga, W., Santillan, M., & Scrivner, C. (2020), Noise characteristics of operational real-time high-rate GNSS positions in a large aperture network. Journal of Geophysical Research: Solid Earth, 125(7), e2019JB019197.

Minson, S. E., Murray, J. R., Langbein, J. O., & Gomberg, J. S. (2014), Real-time inversions for finite fault slip models and rupture geometry based on high-rate GPS data. *Journal of Geophysical Research: Solid Earth*, *119*(4), 3201-3231.

Mousavi, S. M., & Beroza, G. C. (2020a), A machine-learning approach for earthquake magnitude estimation. *Geophysical Research Letters*, *47*(1), e2019GL085976.

Mousavi, S. M., Ellsworth, W. L., Zhu, W., Chuang, L. Y., & Beroza, G. C. (2020b), Earthquake transformer—an attentive deep-learning model for simultaneous earthquake detection and phase picking. *Nature communications*, *11*(1), 1-12.

Murray, J. R., Crowell, B. W., Grapenthin, R., Hodgkinson, K., Langbein, J. O., Melbourne, T., ... & Schmidt, D. A. (2018), Development of a geodetic component for the US West Coast earthquake early warning system. *Seismological Research Letters*, *89*(6), 2322-2336.

Olson, E. L., & Allen, R. M. (2005), The deterministic nature of earthquake rupture. *Nature*, *438*(7065), 212-215 .

Perol, T., Gharbi, M., & Denolle, M. (2018), Convolutional neural network for earthquake detection and location. *Science Advances*, *4*(2), e1700578.

Pitarka, A., Graves, R., Irikura, K., Miyakoshi, K., & Rodgers, A. (2020). Kinematic rupture modeling of ground motion from the M7 Kumamoto, Japan earthquake. *Pure and Applied Geophysics*, *177*(5), 2199-2221.

Riquelme, S., Medina, M., Bravo, F., Barrientos, S., Campos, J., & Cisternas, A. (2018), W-phase real-time implementation and network expansion from 2012 to 2017: The experience in Chile. *Seismological Research Letters*, *89*(6), 2237-2248.

Ross, Z. E., Meier, M. A., Hauksson, E., & Heaton, T. H. (2018), Generalized seismic phase detection with deep learning. *Bulletin of the Seismological Society of America*, *108*(5A), 2894-2901.

Ruhl, C. J., Melgar, D., Geng, J., Goldberg, D. E., Crowell, B. W., Allen, R. M., ... & Cabral-Cano, E. (2019), A global database of strong-motion displacement GNSS recordings and an example application to PGD scaling. *Seismological Research Letters, 90(1), 271-279.*

Ruiz, S., & Madariaga, R. (2018). Historical and recent large megathrust earthquakes in Chile. *Tectonophysics, 733, 37-56.*

Rydelek, P., & Horiuchi, S. (2006), Is earthquake rupture deterministic?. *Nature*, *442*(7100), E5-E6.

Srivastava, N., Hinton, G., Krizhevsky, A., Sutskever, I., & Salakhutdinov, R. (2014), Dropout: a simple way to prevent neural networks from overfitting. The journal of machine learning research, 15(1), 1929-1958 .

Vallée, M., & Douet, V. (2016). A new database of source time functions (STFs) extracted from the SCARDEC method. *Physics of the Earth and Planetary Interiors*, *257*, 149-157.

Williamson, A. L., Melgar, D., Crowell, B. W., Arcas, D., Melbourne, T. I., Wei, Y., & Kwong, K. (2020), Toward near-field tsunami forecasting along the Cascadia subduction zone using rapid GNSS source models. Journal of Geophysical Research: Solid Earth, e2020JB019636.

Wu, Y. M., & Zhao, L. (2006), Magnitude estimation using the first three seconds P-wave amplitude in earthquake early warning. *Geophysical Research Letters*, *33*(16).

Ye, L., Lay, T., Kanamori, H., & Rivera, L. (2016), Rupture characteristics of major and great (Mw≥ 7.0) megathrust earthquakes from 1990 to 2015: 1. Source parameter scaling relationships. *Journal of Geophysical Research: Solid Earth*, *121*(2), 826-844.

Zhu, L., & Rivera, L. A. (2002), A note on the dynamic and static displacements from a point source in multilayered media. Geophysical Journal International, 148(3), 619-627.

Zhu, W., & Beroza, G. C. (2019), PhaseNet: a deep-neural-network-based seismic arrival-time picking method. *Geophysical Journal International*, *216*(1), 261-273.

Supporting information for Early warning for great earthquakes from characterization of crustal deformation patterns with deep learning

J-T., Lin[1], D. Melgar[1], A. M. Thomas[1], and J. Searcy[2]

[1]Department of Earth Sciences, University of Oregon, Eugene, Oregon, USA

[2]Research Advanced Computing Services, University of Oregon, Eugene, Oregon, USA

Corresponding author: Jiun-Ting Lin (jiunting@uoregon.edu)

Contents of this file

Introduction

This supporting information includes details of the rupture scenarios and synthetic waveforms (Text S1), details of the estimated rupture duration (Test S2), and 8 figures supporting the main text.

Text S1. Details on the rupture scenarios and synthetic waveforms

Underpinning the KL expansion method is the notion that slip on a fault can be modeled as a spatially random field (Mai & Beroza, 2002). Once a correlation function is defined then random draws can be made to obtain a stochastic slip pattern. By comparison to slip inversions from earthquakes worldwide several studies have noted that slip is best modeled by the Von Karman correlation function (Mai & Beroza, 2002; Goda et al., 2016; Melgar & Hayes, 2019) where the correlation between the *i*-th and *j*-th subfault in the rupture is defined as

$$C_{ij}(r_{ij}) = \frac{G_H(r_{ij})}{G_0(r_{ij})} \quad (1)$$

$$G_H(r_{ij}) = r_{ij}^H K_H(r_{ij}) \quad (2)$$

where K_H is the modified Bessel function of the second kind and H is the Hurst exponent. We set $H = 0.4$ based on a recent analysis of large earthquakes between 1990 and 2019 (Melgar & Hayes, 2019), which is slightly lower than the value of H=0.7 proposed when stochastic slip models were first employed (Mai & Beroza, 2002; Graves & Pitarka, 2010). $r_{ij}$is the inter-subfault distance given by

$$r_{ij} = \sqrt{(r_s/a_s)^2 + (r_d/a_d)^2} \quad (3)$$

Where r_s is the along-strike distance and $r_d$the along-dip distance. The along-strike and along-dip correlation lengths, a_s and a_d, control the predominant asperity size in the resulting slip pattern (Mai & Beroza, 2002) and scale with indirectly with magnitude as a function of the fault length and width according to

$$a_s = 2.0 + \frac{1}{3}L \quad (4)$$

$$a_d = 1.0 + \frac{1}{3}W \quad (5)$$

Once all the parameters of the correlation matrix are defined the covariance matrix is obtained by

$$\widehat{C_{ij}} = \sigma_i C_{ij} \sigma_j \quad (6)$$

Where $\sigma$is the standard deviation of slip which is usually defined as a fraction of mean slip. Here we set it to 0.9 (LeVeque et al., 2016). Now we can obtain a randomly generated slip pattern with the statistics as defined above by summing the eigenvectors of the covariance matrix according to the K-L expansion(LeVeque et al., 2016) such that

$$s = \mu + \sum_{k=1}^{N} \quad z_k \sqrt{\lambda_k} v_k \quad (7)$$

where s is a column vector containing the values of slip at each of the subfaults for a particular realization. μ is the expected mean slip pattern, we set it to be a vector with enough homogenous slip over the selected subfaults to match the target magnitude. N is the maximum number of summed eigenvectors. We use a reasonably large number of 100 which should give enough variation of slip complexity (Melgar et al., 2016; LeVeque et al., 2016). $z_k$is a scalar randomly selected from a presumed gaussian distribution with mean 0 and standard deviation of 1. λ_k and v_k denotes the eigenvalue and eigenvector of the covariance matrix.

With the stochastic slip pattern in hand, the second step is to define the rupture kinematics. Here we follow common best practices and a full treatment of this can be found in Graves &

Pitarka (2010, 2015). We set the rupture speed to 0.8 of the local shear wave velocity at the subfault depth plus some stochastic perturbation to destroy perfectly circular rupture fronts. The hypocenter is randomly selected from the subfaults that are involved in the rupture to ensure both unilateral and bilateral ruptures. Rise times are defined to be proportional to the square root of local slip (Mena et al., 2010) but over the entire fault model must on average obey known rise-time magnitude scaling laws (Melgar & Hayes, 2017). We then use the Dreger slip rate function to describe the time-evolution at a particular subfault (Mena et al., 2010; Melgar et al., 2016). It is well-known that the shallow megathrust has slow rupture speeds and long rise times, so for subfaults shallower than 10km rupture speeds are set to 0.6 of shear wave speed and rise times are doubled from what is predicted by the scaling by the square root of slip. Below 15km the previously described rules are used, and between 10 and 15km depth a linear transition between the two behaviors is employed. This is similar to what is done for continental strike-slip faults (Graves & Pitarka, 2010). Similarly, the rake vector is set to 90 degrees plus some stochastic perturbations.

Once the slip pattern and its complete time evolution are known, synthetic GNSS waveforms are generated by summing all the synthetic data from participating subfaults. We use the FK package, which is a 1D frequency-wavenumber approach (Zhu & Rivera, 2002) and the LITHO1.0 velocity structure (Pasyanos et al., 2014) to generate the Green's functions from all subfaults to given stations. We focus only on the long period displacement waveforms (<0.5 Hz or 1 second sampling) since they are less sensitive to small scale crustal structure and are the dominant period of large earthquakes.

Text S2. Calculation of estimated rupture duration

We begin the duration estimation by assuming rupture source time function is symmetric (i.e. rise and decline time are the same). Given the Mw-duration scaling of Duputel et al. (2013), duration *T* can be estimated by

$$T = 2.4 \times 10^{-8} \times {M_0}^{1/3}, \quad (8)$$

$$M_0 = 10^{(Mw+10.7)\times 1.5}, \quad (9)$$

Where the M_0 represents moment in dyne-cm. By plugging the equation (9) into (8) with an magnitude Mw-0.3, we can estimate the duration ratio

$$R = (10^{(Mw-0.3+10.7)\times 1.5} / 10^{(Mw+10.7)\times 1.5})^{1/3} = 71\% \quad (10)$$

Thus, the duration of Mw-0.3 can be estimated by 71% of the original Mw duration.

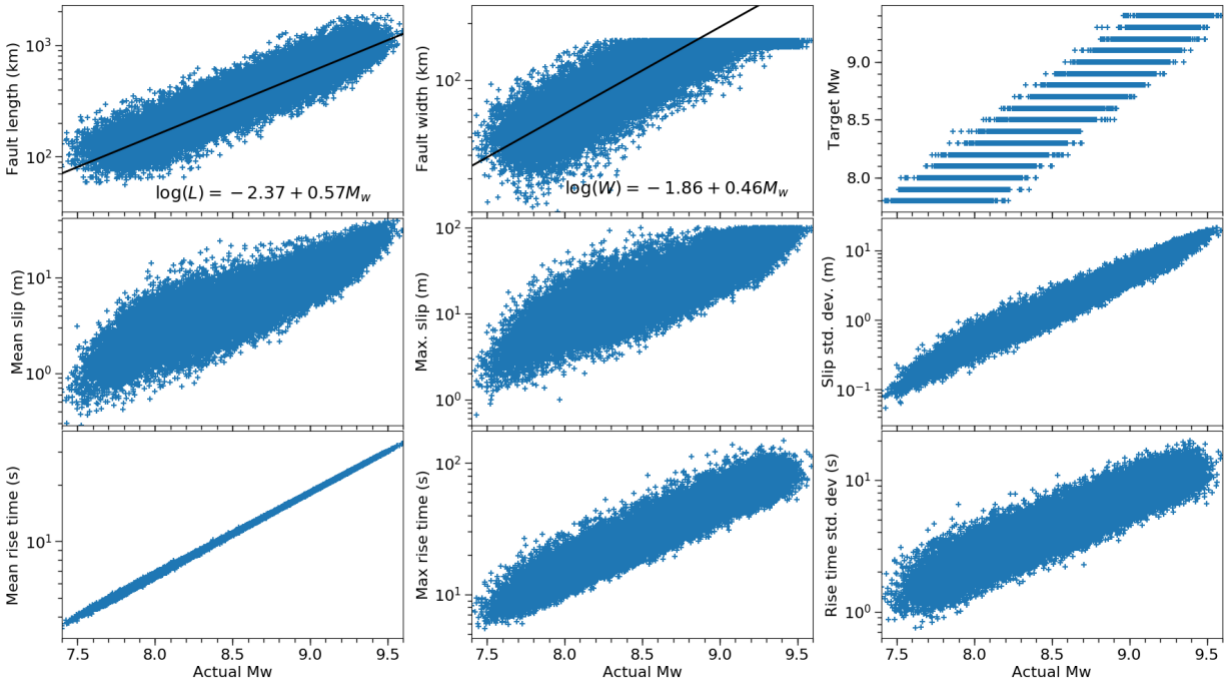

Figure S1. *Source parameters for the 27200 rupture scenarios.*

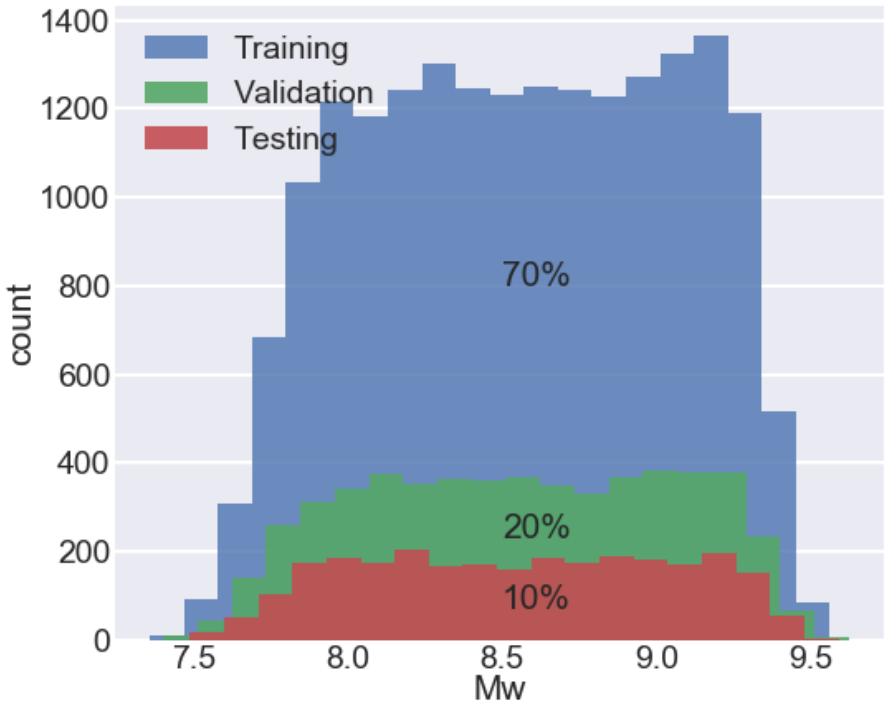

***Figure S2**. Histogram and partition of training, validation and testing dataset.*

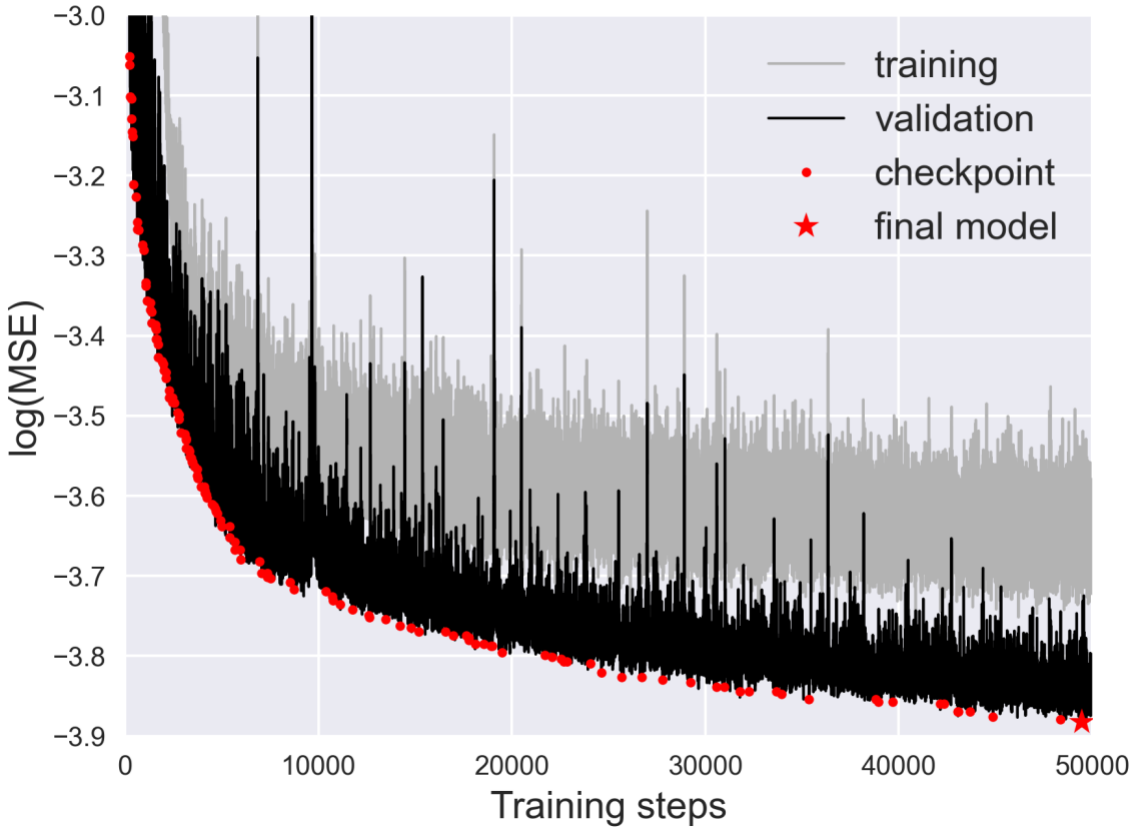

Figure S3. *Training curve for M-LARGE. Light and dark line show the MSE for training and validation data, respectively. Red dots denote the checkpoints for the training, with interval of every 5 epochs and save the model if the current checkpoint loss is smaller than the previous checkpoint loss. Red star represents the final selected model, which has the minimum checkpoint loss. Note that the validation loss is smaller than the training loss because dropouts are only implemented in the loss calculation.*

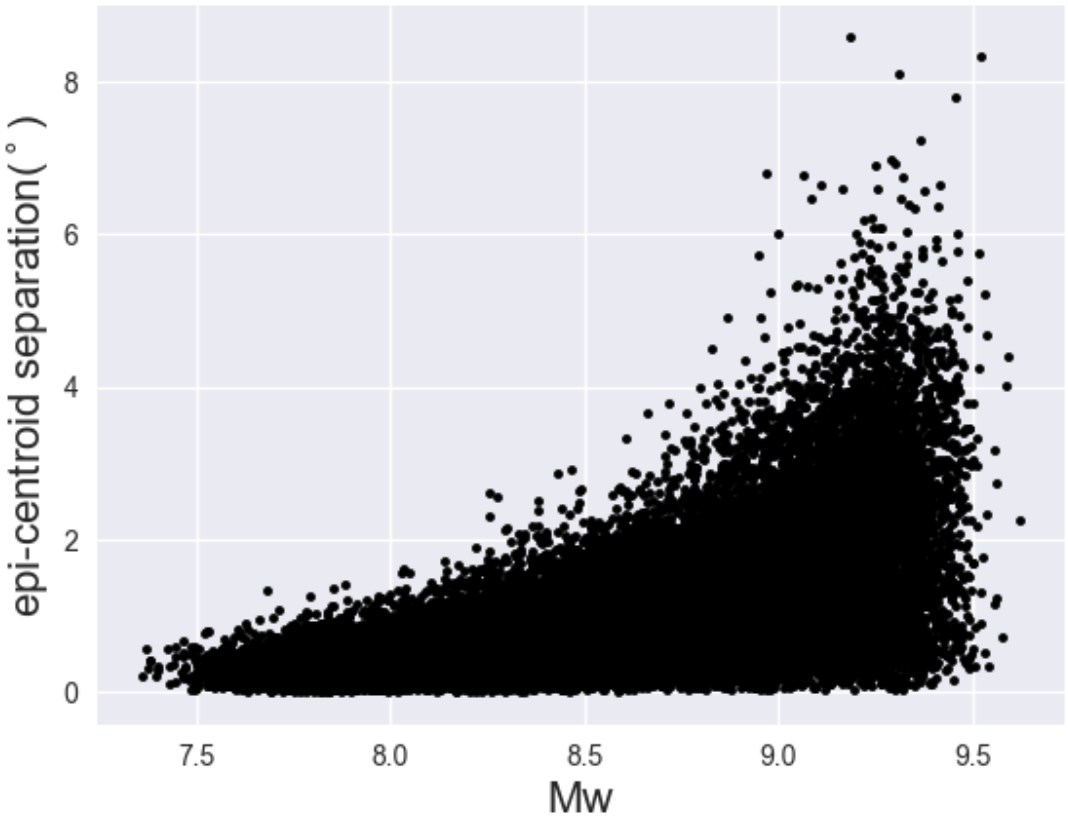

Figure S4*. Epicenter and centroid separation for all the 27200 rupture scenarios.*

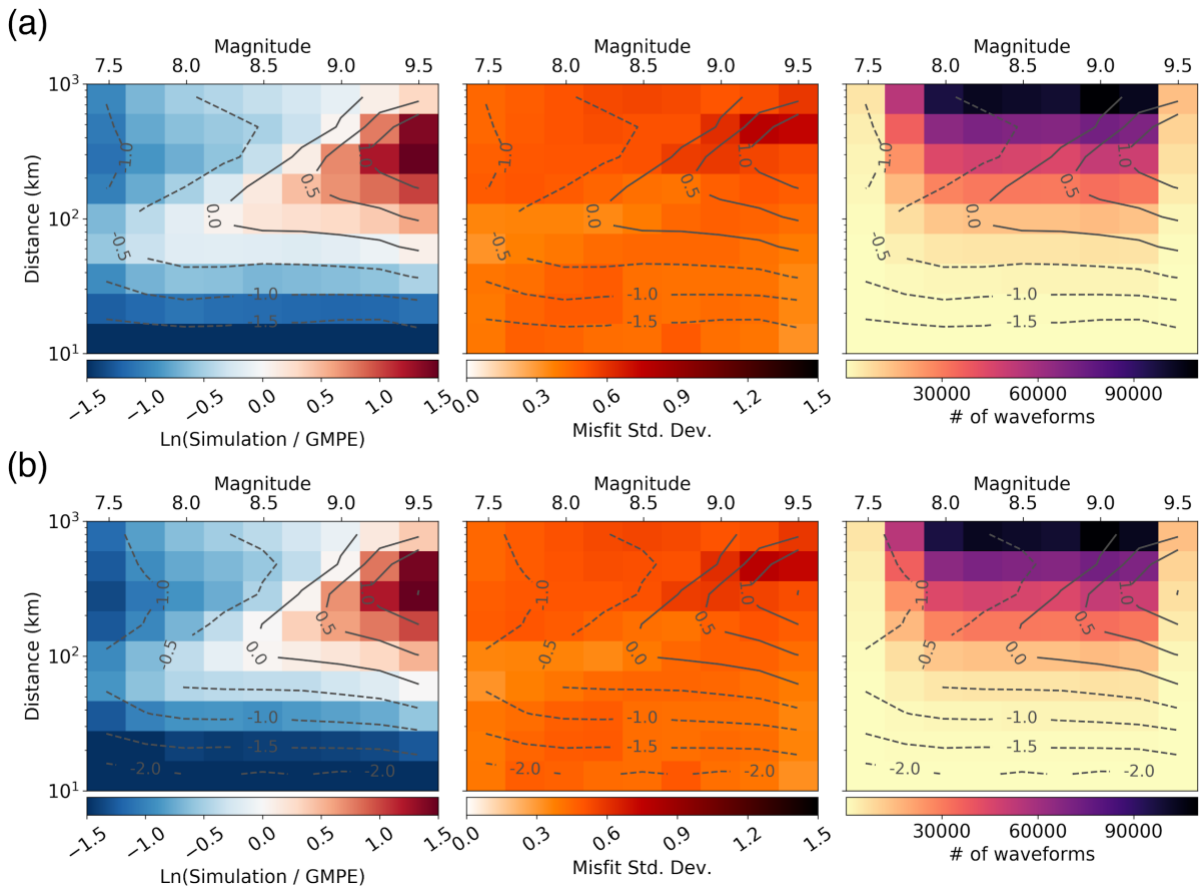

***Figure S5**. Comparison between synthetic data and PGD-Mw scaling of (a) Melgar et al. (2015) and (b) Ruhl et al. (2019). (a) and (b) from left to right shows the misfit of synthetic PGD and PGD-Mw scaling and its contour; standard deviation of the misfit; and distribution of waveforms in count.*

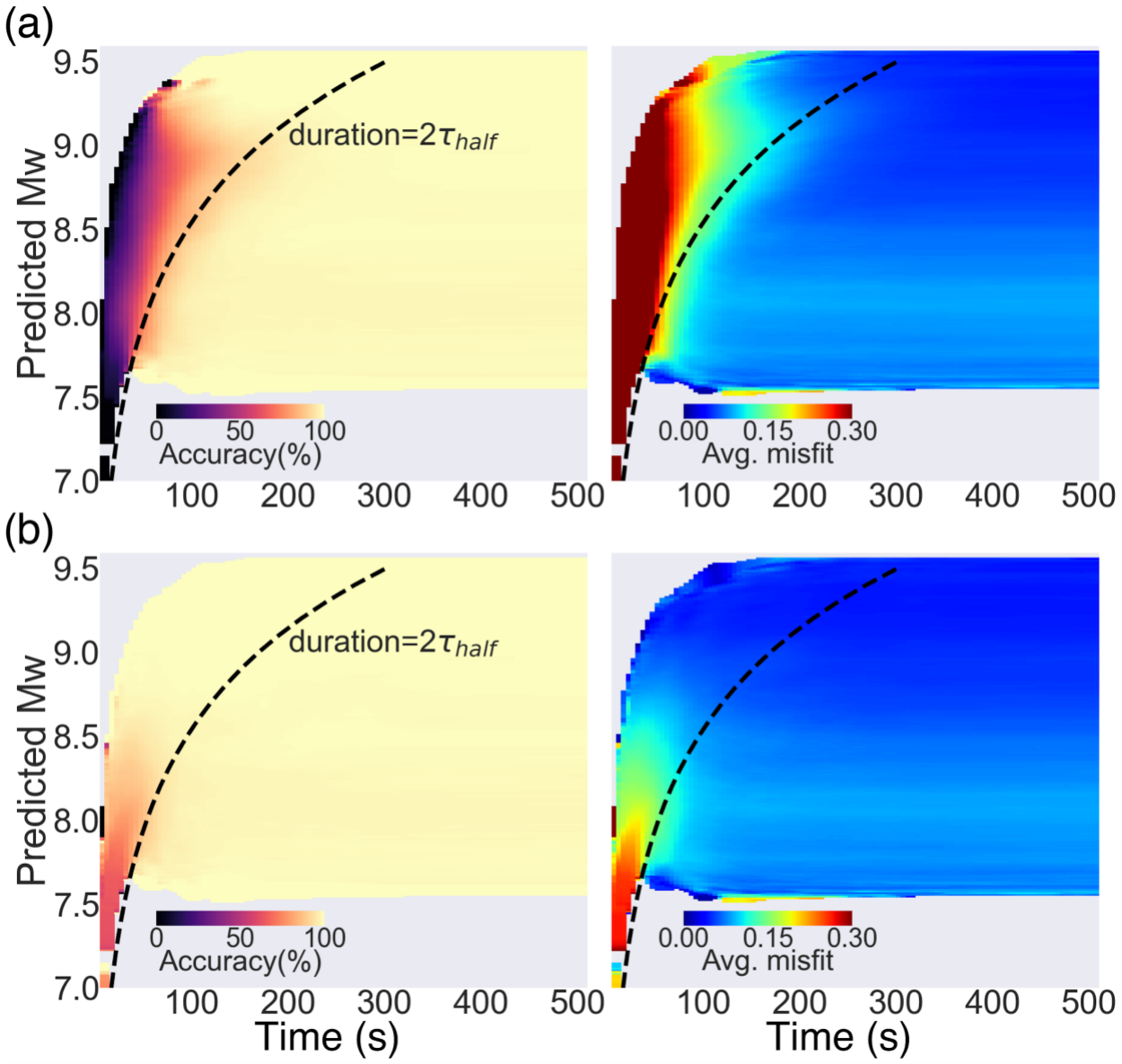

Figure S6. *Model performance for testing dataset. (a) shows the prediction accuracy (i.e. number of success prediction/total samples) as a function of time and Mw. Where a success prediction is defined as when the predicted and final Mw misfit is <0.3. Dashed line shows the estimated duration. (b) same as (a), but define a success prediction is when the predicted and time dependent Mw misfit is <0.3. Note that the time dependent Mw is the integration from the STF at current time.*

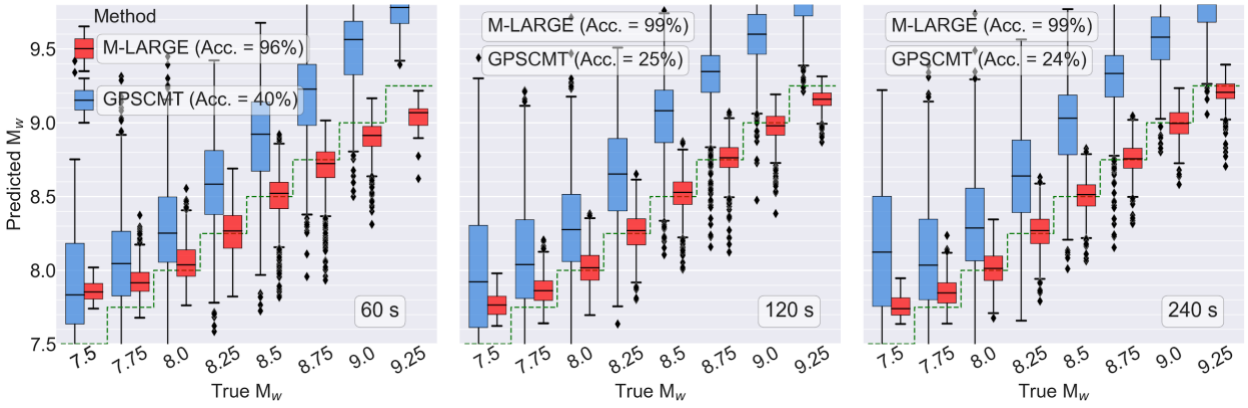

Figure S7. *Similar to the Fig. 2b, but the comparison of the M-LARGE (red) and GPSCMT (blue) predicted magnitudes at 60,120 and 240 s for different magnitude bins. Model accuracies at 60, 120 and 240 s are shown in text. The green dashed lines show the 1:1 reference for each magnitude bin.*

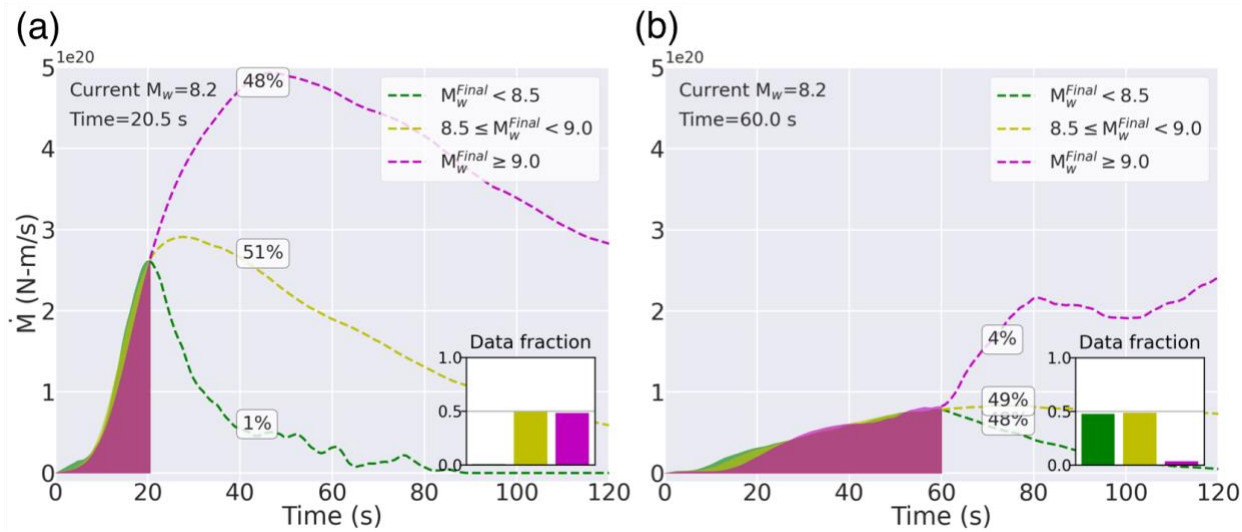

Figure S8. *Example STFs in our dataset showing the sources are not strongly deterministic but some degree of weak determinism. (a) The STFs at 20.5 s have similar shapes and accumulated Mw of 8.2, however, are ambiguous to their final magnitude. The percentage texts denote the fractions of data that eventually grow to the designated groups. Dashed lines show the averaged future STFs for each group. (b) same as (a) but show the STFs at 60 s. The statistic shows it is less likely (i.e. 4%) that an event can grow to a very large event although some large Mw earthquakes take hundreds of seconds to rupture. The possibility is limited according to the current rupture history and the remaining available space of growth limited by the subduction zone geometry.*

References

Duputel, Z., Tsai, V. C., Rivera, L., & Kanamori, H. (2013). Using centroid time-delays to characterize source durations and identify earthquakes with unique characteristics. *Earth and Planetary Science Letters*, *374*, 92-100.

Goda, K., Yasuda, T., Mori, N., & Maruyama, T. (2016), New scaling relationships of earthquake source parameters for stochastic tsunami simulation. Coastal Engineering Journal, 58(3), 1650010-1.

Graves, R. W., & Pitarka, A. (2010), Broadband ground-motion simulation using a hybrid approach. Bulletin of the Seismological Society of America, 100(5A), 2095-2123.

Graves, R., & Pitarka, A. (2015), Refinements to the Graves and Pitarka (2010) broadband ground-motion simulation method. Seismological Research Letters, 86(1), 75-80.

LeVeque, R. J., Waagan, K., González, F. I., Rim, D., & Lin, G. (2016), Generating random earthquake events for probabilistic tsunami hazard assessment. In Global Tsunami Science: Past and Future, Volume I (pp. 3671-3692). Birkhäuser, Cham.

Mai, P. M., & Beroza, G. C. (2002), A spatial random field model to characterize complexity in earthquake slip. Journal of Geophysical Research: Solid Earth, 107(B11), ESE-10.

Melgar, D., LeVeque, R. J., Dreger, D. S., & Allen, R. M. (2016), Kinematic rupture scenarios and synthetic displacement data: An example application to the Cascadia subduction zone. *Journal of Geophysical Research: Solid Earth*, *121*(9), 6658-6674.

Melgar, D., & Hayes, G. P. (2017), Systematic observations of the slip pulse properties of large earthquake ruptures. *Geophysical Research Letters*, *44*(19), 9691-9698.

Melgar, D., & Hayes, G. P. (2019), The correlation lengths and hypocentral positions of great earthquakes. Bulletin of the Seismological Society of America, 109(6), 2582-2593.

Mena, B., Mai, P. M., Olsen, K. B., Purvance, M. D., & Brune, J. N. (2010), Hybrid broadband ground-motion simulation using scattering Green's functions: Application to large-magnitude events. Bulletin of the Seismological Society of America, 100(5A), 2143-2162.

Pasyanos, M. E., Masters, T. G., Laske, G., & Ma, Z. (2014), LITHO1. 0: An updated crust and lithospheric model of the Earth. *Journal of Geophysical Research: Solid Earth, 119(3), 2153-2173.*

Zhu, L., & Rivera, L. A. (2002), A note on the dynamic and static displacements from a point source in multilayered media. Geophysical Journal International, 148(3), 619-627.